

RESEARCH

Open Access



# Bioinformatic identification and experiment validation reveal 6 hub genes, promising diagnostic and therapeutic targets for Alzheimer's disease

Wenyuan Cao<sup>1</sup>, Zhangge Ji<sup>1</sup>, Shoulian Zhu<sup>1</sup>, Mei Wang<sup>2</sup> and Runming Sun<sup>1\*</sup>

## Abstract

**Background** Alzheimer's disease (AD) is a progressive neurodegenerative disease that can cause dementia. We aim to screen out the hub genes involved in AD based on microarray datasets.

**Methods** Gene expression profiles GSE5281 and GSE28146 were retrieved from Gene Expression Omnibus database to acquire differentially expressed genes (DEGs). Gene Ontology and pathway enrichment were conducted using DAVID online tool. The STRING database and Cytoscape tools were employed to analyze protein-protein interactions and identify hub genes. The predictive value of hub genes was assessed by principal component analysis and receiver operating characteristic curves. AD mice model was constructed, and histology was then observed by hematoxylin-eosin staining. Gene expression levels were finally determined by real-time quantitative PCR.

**Results** We obtained 197 overlapping DEGs from GSE5281 and GSE28146 datasets. After constructing protein-protein interaction network, three highly interconnected clusters were identified and 6 hub genes (*RBL1*, *BUB1*, *HDAC7*, *KAT5*, *SIRT2*, and *ITGB1*) were selected. The hub genes could be used as basis to predict AD. Histological abnormalities of brain were observed, suggesting successful AD model was constructed. Compared with the control group, the mRNA expression levels of *RBL1*, *BUB1*, *HDAC7*, *KAT5* and *SIRT2* were significantly increased, while the mRNA expression level of *ITGB1* was significantly decreased in AD groups.

**Conclusion** *RBL1*, *BUB1*, *HDAC7*, *KAT5*, *SIRT2* and *ITGB1* are promising gene signatures for diagnosis and therapy of AD.

**Keywords** Alzheimer disease, Gene expression profiling, Protein interaction maps, Computational biology

## Introduction

Alzheimer's disease (AD), also known as senile dementia, is a common neurodegenerative disease that causes cognitive decline and dementia [1, 2]. During the past 20 years, the number of reported deaths induced by AD has been hugely increased [3]. There are over 50 million people globally with AD and the number of people with AD will exceed 100 million in 2050 [4]. The main cause of AD is the accumulation of beta-amyloid protein and misfolded microtubule-associated tau protein molecules in AD patients, damage nerves and other brain cells, which

\*Correspondence:

Runming Sun  
runmingsun@126.com

<sup>1</sup> Department of Neurology Second Ward, Zibo Municipal Hospital, No. 139, Huangong Road, Linzi District, Zibo City 255400, Shandong Province, China

<sup>2</sup> Department of Rehabilitation, Zibo Municipal Hospital, No. 139, Huangong Road, Linzi District, Zibo City 255400, Shandong Province, China



© The Author(s) 2023. **Open Access** This article is licensed under a Creative Commons Attribution 4.0 International License, which permits use, sharing, adaptation, distribution and reproduction in any medium or format, as long as you give appropriate credit to the original author(s) and the source, provide a link to the Creative Commons licence, and indicate if changes were made. The images or other third party material in this article are included in the article's Creative Commons licence, unless indicated otherwise in a credit line to the material. If material is not included in the article's Creative Commons licence and your intended use is not permitted by statutory regulation or exceeds the permitted use, you will need to obtain permission directly from the copyright holder. To view a copy of this licence, visit <http://creativecommons.org/licenses/by/4.0/>. The Creative Commons Public Domain Dedication waiver (<http://creativecommons.org/publicdomain/zero/1.0/>) applies to the data made available in this article, unless otherwise stated in a credit line to the data.

can lead to neuronal cell death and brain injury [5, 6]. Additionally, immune activation and astrocytic and glial cell-mediated neuroinflammation have been implicated in the pathogenesis of AD [7–9]. Only two medication classes—cholinesterase inhibitors and N-methylD-aspartate antagonists—are currently licensed for the treatment of AD [10]. Finding new therapeutic targets is urgently needed due to the limited treatments for AD.

Microarray analysis and gene sequencing have been widely applied to explore the potential biomarkers or therapeutic targets of AD. After using 3 microarray datasets to screen mitogen-related hub genes in peripheral blood mononuclear cells of AD patients, 53 differentially expressed genes (DEGs) of AD are identified, which may serve as possible biomarkers for the diagnosis of AD [11]. LncRNA RP11-59J16.2 may be a molecular target for AD, according to microarray analysis of blood from AD patients and healthy controls to determine LncRNA and mRNA expression profiles [12]. After applying bioinformatics tools to analyze microarray profiling, nine blood-related differentially expressed miRNAs are identified, with potential as diagnostic biomarkers at an early stage [13]. Therefore, it is an important approach to explore and identify novel biomarkers and therapeutic targets associated with AD by screening for gene and molecular network changes related to the onset and progression of AD. However, the gene signature of AD has not been deeply explored.

In this study, we determined 6 hub genes of AD based on GSE5281 and GSE28146 datasets. And the expression of hub genes was further confirmed by constructing AD mouse model. The purpose of this investigation is to offer new knowledge on the molecular causes and gene biomarkers of AD.

## Materials and methods

### Expression profile datasets

The gene expression profiles we used were obtained from Gene Expression Omnibus (GEO) database <https://www.ncbi.nih.gov/geo/>. Datasets related to “Alzheimer’s disease” were retrieved, and two microarray datasets (GSE5281 and GSE28146) that met the criteria were selected.

### DEGs selection

The microarray data of the two datasets retrieved from the GEO database were conducted using the GEO2R ([www.ncbi.nlm.nih.gov/geo/geo2r](http://www.ncbi.nlm.nih.gov/geo/geo2r)). DEGs were screened out according to a significance threshold with  $BH < 0.05$  ( $BH$ :  $P$  value corrected by Benjamini-Hochberg multiple test) and  $|\log FC| \geq 1.5$  (AD vs. Control). Heatmaps and volcano plots were plotted to visualize the identified DEGs. The samples of datasets were standardized

and normalized using boxplots for data correction. Venn diagrams were created using Draw Venn Diagram tool (<http://bioinformatics.psb.ugent.be/webtools/Venn/>) to display the common DEGs between GSE5281 and GSE28146 datasets.

### Functional and pathway enrichment analysis

The Database for Annotation, Visualization and Integrated Discovery (DAVID) database was applied to carry out Gene Ontology (GO) and Kyoto Encyclopedia of Genes and Genomes (KEGG) enrichment analysis. Then, the GO and KEGG enrichment results were performed using R language. The most significantly enriched top 6 GO terms with the minimum adjusted  $p$ -values of each category and the top 8 significantly enriched pathways with the minimum adjusted  $p$ -value were selected for display, and enrichment analysis bar charts and bubble charts were created.

### Protein–protein interaction (PPI) network construction and hub gene identification

The STRING (<https://www.string-db.org/>) online database was employed to predict the PPI of DEGs. The significance level was set at a confidence interaction score of 0.4. Subsequently, the PPI network was displayed using Cytoscape software ([www.cytoscape.org/](http://www.cytoscape.org/)). MCODE (Molecular Complex Detection) was employed to identify key modules from the PPI network of DEGs. The degree of each protein node was determined using the Cytoscape plugin CytoHubba Version 0.1 to filter out hub genes based on the connectivity.

### Hub gene analysis

A GO enrichment chord diagram was drawn to reveal the differences of hub genes in biological functions using R package ggplot2. The expression levels of hub genes in GSE28146 dataset were used as variables for principal component analysis (PCA). Two principal component variables, PC1 and PC2A were obtained after processing R language. The expression ridge plot was drawn using R language. Gene expression profile interactive analysis (<http://gepia.cancer-pku.cn/>) was applied to create a receiver operating characteristic (ROC) curve to assess the diagnostic accuracy of the hub genes according to the area under the curve (AUC).

### AD mouse model construction

ICR male mice (SPF Biotechnology Co.,Ltd., Beijing, China) at the age of 6–8 weeks, weighing 19–21 g, were separated into control group and model group (6 mice per group). After 1 week of adaptive feeding, the mice were intraperitoneally injected with 0.1 mL scopolamine at a daily dose of 1.5 mg/kg for 15 d to establish the model

of AD. Mice were euthanized by intraperitoneal injection of 0.3% sodium pentobarbital (30 mg/kg body weight) and the brain tissue was extracted for subsequent assay.

Each mouse received unlimited food and was housed in a pathogen-free environment. The ethics committee gave the approval to the methods for caring for and using animals, and all relevant institutional and governmental guidelines for the ethical use of animals were followed.

**Real-time fluorescence quantitative PCR (RT-qPCR)**

Total RNA was extracted from brain tissues using the TRIZOL reagent (Invitrogen, Carlsbad, CA, USA). A UV spectrophotometer was employed to measure the absorbance values at 260nm and 280nm to calculate the concentration of total RNA diluted 20 times with RNA se-free water. High purity samples (OD 260/OD 280 ratio

between 1.9 and 2.0) were suitable for the following studies. Reverse transcription to synthesize cDNA templates was performed using a PCR amplification instrument. RT-qPCR were conducted using an ABI7500 Quantitative PCR instrument (Applied Biosystems, Foster City, CA, USA) with the following reaction procedures: pre-denaturation at 95°C for 30s, denaturation at 95°C for 10s, annealing at 60°C for 30s, and 40 cycles. GAPDH was used as an internal reference. The obtained Ct values were analyzed using the  $2^{-\Delta\Delta Ct}$  method. Each experiment was repeated three times. The primer sequences were listed in Table S1.

**Hematoxylin-eosin (HE) staining**

The mouse brain tissue was fixed in a 4% paraformaldehyde solution. The next day, after washing away

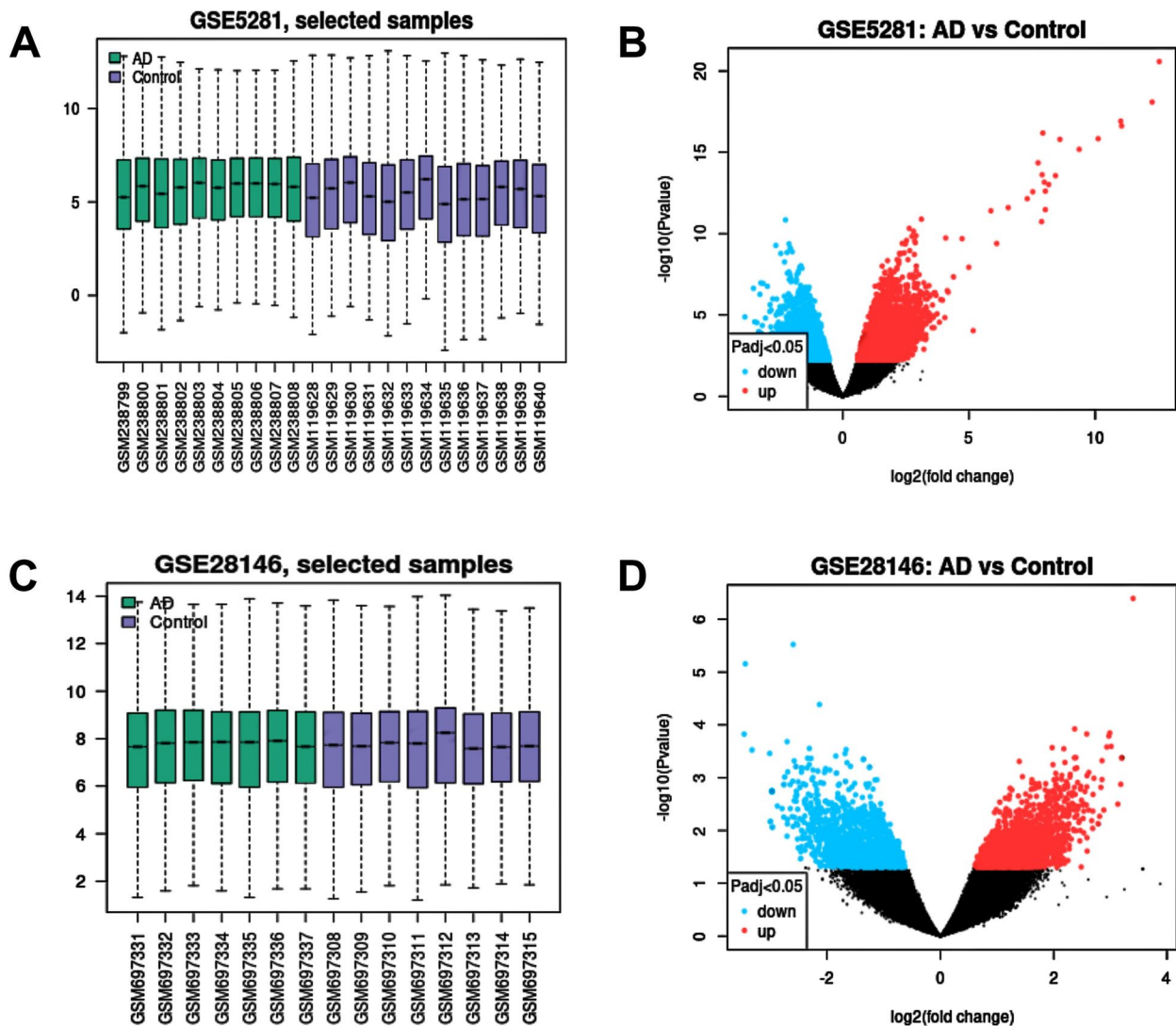


**Fig. 1** a, c Box plots of the data normalization results for the dataset samples. b, d Volcano plots with log<sub>2</sub> Fold Change as the x-axis and -log<sub>10</sub> (p-value) as the y-axis. Red dots represent up-regulated genes, and blue dots represent down-regulated genes

paraformaldehyde solution, and the tissue was dehydrated using a gradient of 50–70% - 80 - 90% - 95% ethanol. Then the tissue was placed in a mixture of 1:1 ethanol and xylene for 30min, and then transferred to pure xylene for transparency. The tissue was embedded in a paraffin solution. The paraffin portions were in an oven at 60°C and roasted for 2h and dewaxed from xylene to water using routine xylene and ethanol treatments. Sections were stained with hematoxylin and eosin for 10min and observed using an optical microscope.

### Statistical analysis

Data processing was conducted using GraphPad Prism 7.0, which were presented as mean  $\pm$  standard deviation. Comparisons between two groups were conducted by t-test, and  $P < 0.05$  showed a statistical significance.

## Results

### Microarray data and DEGs identification

Two gene expression profile datasets were selected for this study, GSE5281 and GSE28146. After normalization and removal of batch effects, we selected total 23 samples in GSE5281 and 15 samples in GSE28146 for further analysis (Fig. 1a, c). The gene dataset GSE5281 consisted of 13 normal brain samples (Control) and 10 AD samples. Using GEO2R, 2780 DEGs were isolated in GSE5281, with 2198 up-regulated genes and 582 down-regulated

genes. The GSE28146 dataset included 8 normal brain samples (Control) and 7 AD samples. There were 1123 DEGs were identified, among which 604 genes were up-regulated and 519 genes were down-regulated. Clustering analysis was performed on DEGs from both datasets and generated the volcano plots (Fig. 1b, d).

A Venn diagram revealed that there were 197 common DEGs between the GSE5281 dataset and the GSE28146 dataset (Fig. 2a). Subsequently, the top 25 significantly up-regulated and down-regulated DEGs were selected, and a heatmap was created for visualization (Table 1) (Fig. 2b).

### Functional enrichment analysis of common DEGs

The molecular function (MF), biological process (BP), and cellular component (CC) categories grouped the results of the GO enrichment study. The GO enrichment analysis bubble plot and the GO enrichment analysis bar plot displayed the top 6 notably enriched GO terms (Fig. 3a, b). For the MF, the DEGs mainly enriched in “transcription factor binding”, “protein binding”, “transcription factor activity”, “chromatin binding”, “transcriptional activator activity”, “calmodulin binding”. For the BP, the DEGs mainly enriched in “positive regulation of transcription, DNA-templated”, “positive regulation of transcription from RNA polymerase II promoter”, “cell morphogenesis”, “macromolecular complex assembly”, “cell adhesion”, “negative regulation of

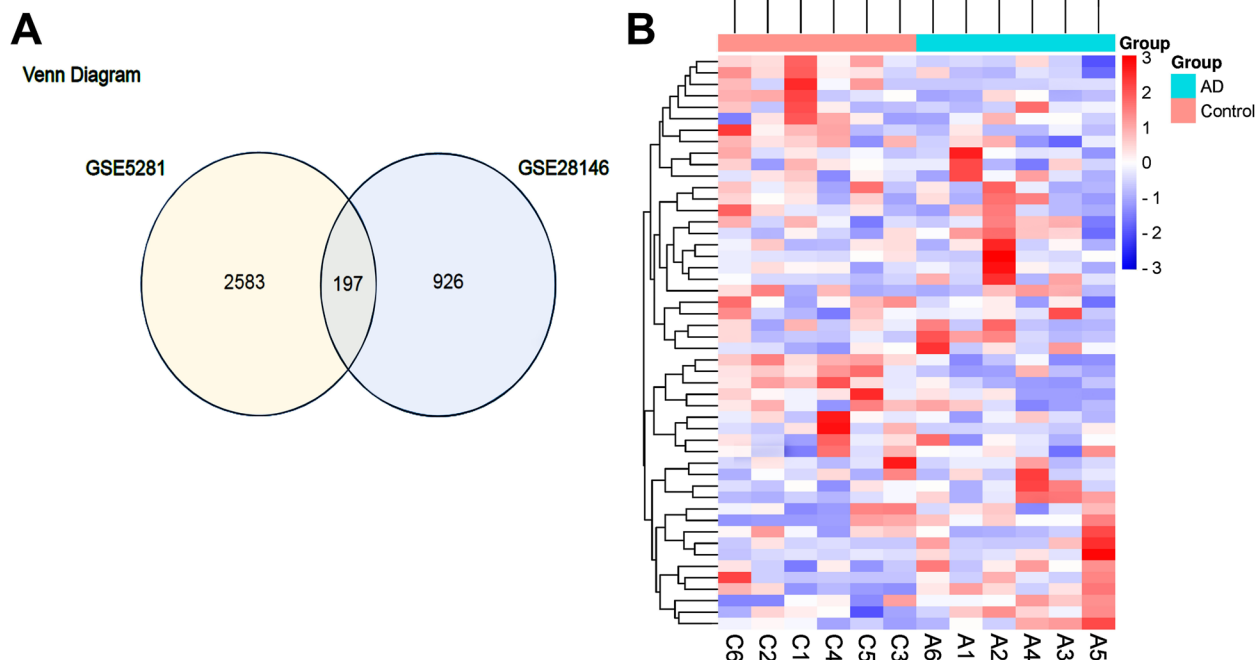


**Fig. 2** a Venn diagram of common differentially expressed genes (DEGs). The sum of the numbers of each circle represents the total number of DEGs, and the overlapping regions indicate the common DEGs between comparison groups. b Heatmap representation of the selected genes. Each column represents a sample and the horizontal axis represents genes. Red indicates high expression, and blue indicates low expression

**Table 1** Common differentially expressed gene of GSE5281 and GSE28146 datasets

Name	Description	log2FoldChange	pval	up/down
YME1L1	YME1 like 1 ATPase	2.97	1.63E-04	up
KMT2A	lysine methyltransferase 2A	2.69	4.30E-03	up
C10orf90	chromosome 10 open reading frame 90	2.62	7.98E-04	up
EGFR	epidermal growth factor receptor	2.49	4.91E-02	up
FARP2	FERM, ARH/RhoGEF and pleckstrin domain protein 2	2.44	3.46E-03	up
CMYA5	cardiomyopathy associated 5	2.38	2.07E-03	up
NSUN3	NOP2/Sun RNA methyltransferase family member 3	2.31	1.45E-02	up
MAG11	membrane associated guanylate kinase, WW and PDZ domain containing 1	2.28	3.57E-03	up
LOC101927027	uncharacterized LOC101927027	2.25	4.95E-03	up
NPAS3	neuronal PAS domain protein 3	2.23	1.36E-02	up
SLC25A37	solute carrier family 25 member 37	2.22	4.05E-03	up
NFYA	nuclear transcription factor Y subunit alpha	2.21	8.77E-03	up
SESN2	sestrin 2	2.19	2.80E-03	up
PIK3C2A	phosphatidylinositol-4-phosphate 3-kinase catalytic subunit type 2 alpha	2.17	3.42E-02	up
PARD3B	par-3 family cell polarity regulator beta	2.16	5.22E-03	up
PAX8	paired box 8	2.15	3.87E-03	up
OR5J2	olfactory receptor family 5 subfamily J member 2	2.15	3.63E-03	up
IQSEC3	IQ motif and Sec7 domain 3	2.14	1.07E-03	up
EP400	E1A binding protein p400	2.13	3.60E-02	up
DOCK9	dedicator of cytokinesis 9	2.12	2.88E-02	up
MAP3K6	mitogen-activated protein kinase kinase kinase 6	2.08	1.21E-02	up
PHF19	PHD finger protein 19	2.06	8.62E-03	up
BUB1	BUB1 mitotic checkpoint serine/threonine kinase	2.05	1.77E-02	up
ELK4	ELK4, ETS transcription factor	2.04	5.34E-03	up
PRB1	proline rich protein BstNI subfamily 1	2.04	8.28E-04	up
EIF1AY	eukaryotic translation initiation factor 1A, Y-linked	-2.71	1.28E-02	down
MYH11	myosin heavy chain 11	-2.58	4.80E-04	down
MIR4683//FZD8	microRNA 4683//frizzled class receptor 8	-2.54	7.25E-03	down
COL11A1	collagen type XI alpha 1 chain	-2.46	2.52E-02	down
LOC100996385	uncharacterized LOC100996385	-2.45	7.87E-04	down
DUSP16	dual specificity phosphatase 16	-2.37	2.53E-03	down
FBXL17	F-box and leucine rich repeat protein 17	-2.37	1.40E-02	down
KIAA1841	KIAA1841	-2.33	7.73E-03	down
SLF2	SMC5-SMC6 complex localization factor 2	-2.28	4.31E-04	down
TMLHE	trimethyllysine hydroxylase, epsilon	-2.28	7.54E-03	down
VPS53	VPS53, GARP complex subunit	-2.25	8.13E-03	down
CDH7	cadherin 7	-2.14	2.08E-02	down
MYLIP	myosin regulatory light chain interacting protein	-2.13	9.11E-03	down
CAMSAP1	calmodulin regulated spectrin associated protein 1	-2.11	3.82E-03	down
SCFD1	sec1 family domain containing 1	-2.07	1.43E-02	down
CEP350	centrosomal protein 350	-2.06	1.12E-02	down
NMNAT2	nicotinamide nucleotide adenyltransferase 2	-2.06	1.22E-02	down
DRP2	dystrophin related protein 2	-2.04	2.51E-02	down
TMF1	TATA element modulatory factor 1	-2.03	2.20E-02	down
CACNG4	calcium voltage-gated channel auxiliary subunit gamma 4	-2.03	6.73E-04	down
ARHGEF28	Rho guanine nucleotide exchange factor 28	-2.02	3.06E-02	down
FAM86B3P	family with sequence similarity 86, member A pseudogene	-2.02	2.45E-02	down
IKZF3	IKAROS family zinc finger 3	-2.00	2.24E-02	down
UBASH3B	ubiquitin associated and SH3 domain containing B	-1.97	1.34E-02	down
NELFCD	negative elongation factor complex member C/D	-1.97	1.85E-02	down

transcription from RNA polymerase II promoter”. And for the CC, the DEGs mainly enriched in “cytosol”, “nucleoplasm”, “endosome membrane”, “chromatin”, “glial cell projection”, “ruffle membrane”.

Based on the KEGG enrichment analysis results of the DEGs, the top 8 enriched pathways were displayed in the KEGG pathway enrichment analysis bubble plot and the KEGG enrichment analysis bar plot, which mainly enriched in “MAPK signaling pathway”, “human papillomavirus infection”, “transcriptional mis regulation in cancer”, “proteoglycans in cancer”, “Rap1 signaling pathway”, “pathways in cancer”, etc. (Fig. 3c, d).

**PPI construction and key module analysis**

Utilizing the STRING tool, a PPI network based on DEGs was constructed (Fig. S1A). Subsequently, MCODE

(Molecular Complex Detection) was used to identify three highly interconnected clusters from the PPI network of DEGs, which potentially represented functional molecular complexes associated with AD. *RBL1*, *BUB1*, *HDAC7*, *KAT5*, *SIRT2* and *ITGB1* were selected as hub genes from these molecular (Fig. S1B).

**Analysis of hub genes**

We used R language to create a GO enrichment chord diagram, which revealed the differences of hub genes in biological functions and the relationship between protein and pathway of hub genes. The left side of the GO enrichment chord diagram was the hub gene sequenced according to Log Fold Change, and the right side was the GO term list. The hub gene with the significantly up-regulated differential fold was *BUB1*, and the hub

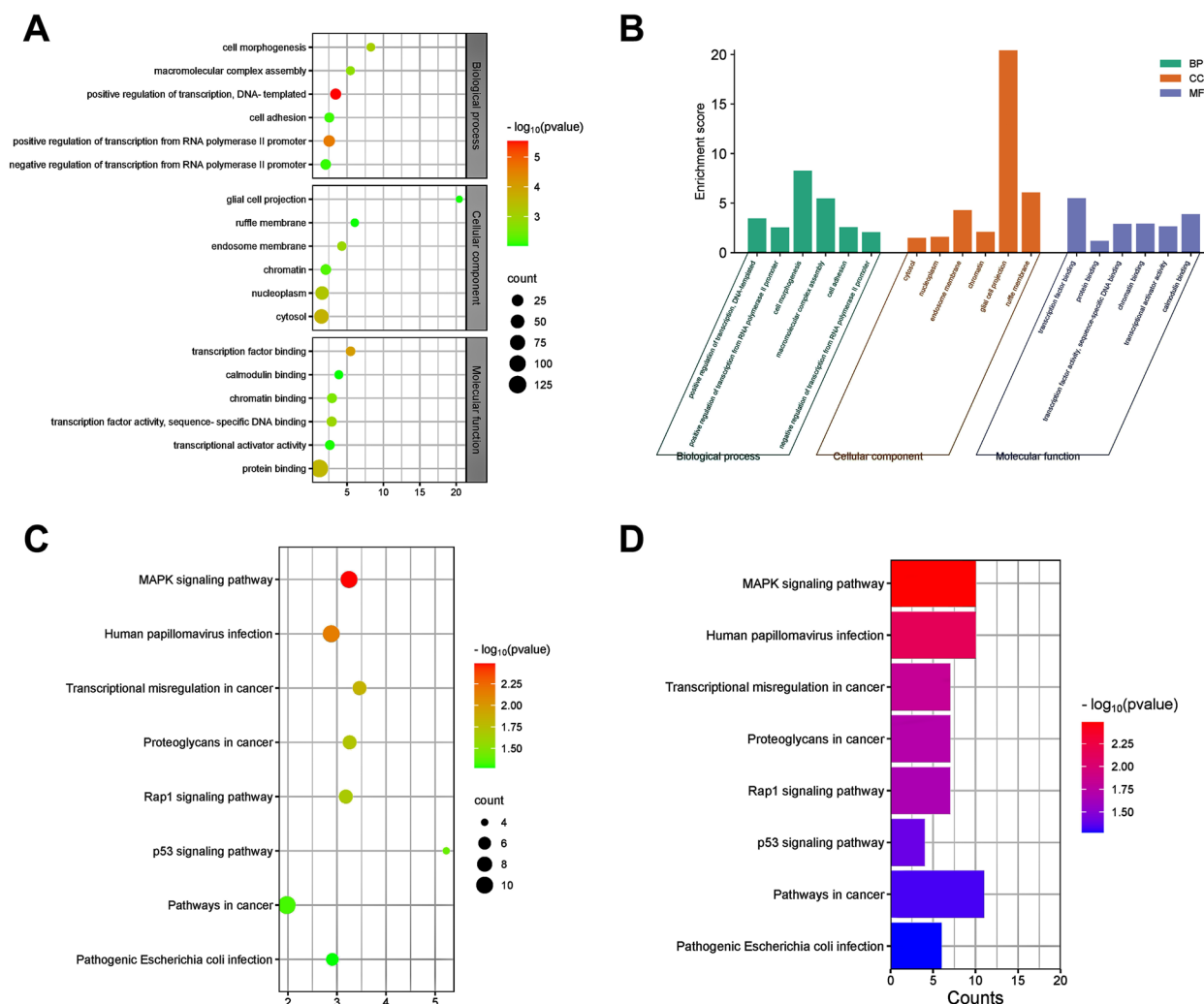


**Fig. 3** Enrichment analysis of the common DEGs. **A** Gene Ontology (GO) enrichment analysis bubble plot. The color intensity of nodes represents the adjusted *p*-value, and the node size indicates the number of genes. **B** GO enrichment analysis bar plot. The x-axis represents the GO terms, and the y-axis represents the  $-\log_{10}(p\text{-value})$  of enrichment of each term. **C** Kyoto Encyclopedia of Genes and Genomes (KEGG) bubble plot. **D**: KEGG bar plot

gene with the significantly down-regulated differential fold was *ITGB1*. The biological process of the hub genes was mainly enriched in “gastrin signaling pathway”, “mitotic cell cycle process”, “regulation of chromosome” and “chromatin organization” (Fig. 4a).

PCA analysis revealed that hub genes were the key influencing factors of AD (Fig. 4b). The scatter plot (PC1 and PC2 as the horizontal and vertical coordinates) suggested the total variance explained rate of PC1 and PC2 was 69.5% and the samples had a good

separation, further confirming the effectiveness of PC1 and PC2, which indicating that hub genes could distinguish between the AD samples from control samples. To visualize the expression level of hub genes in the original sample, we plotted the ridgeline plot using R language, showing the distribution of hub gene expression (Fig. 4c). These indicators could serve as a basis for distinguishing between control samples and AD samples.

The ROC curves of *RBL1*, *BUB1*, *HDAC7*, *KAT5*, *SIRT2*, and *ITGB1* were plotted using raw data from

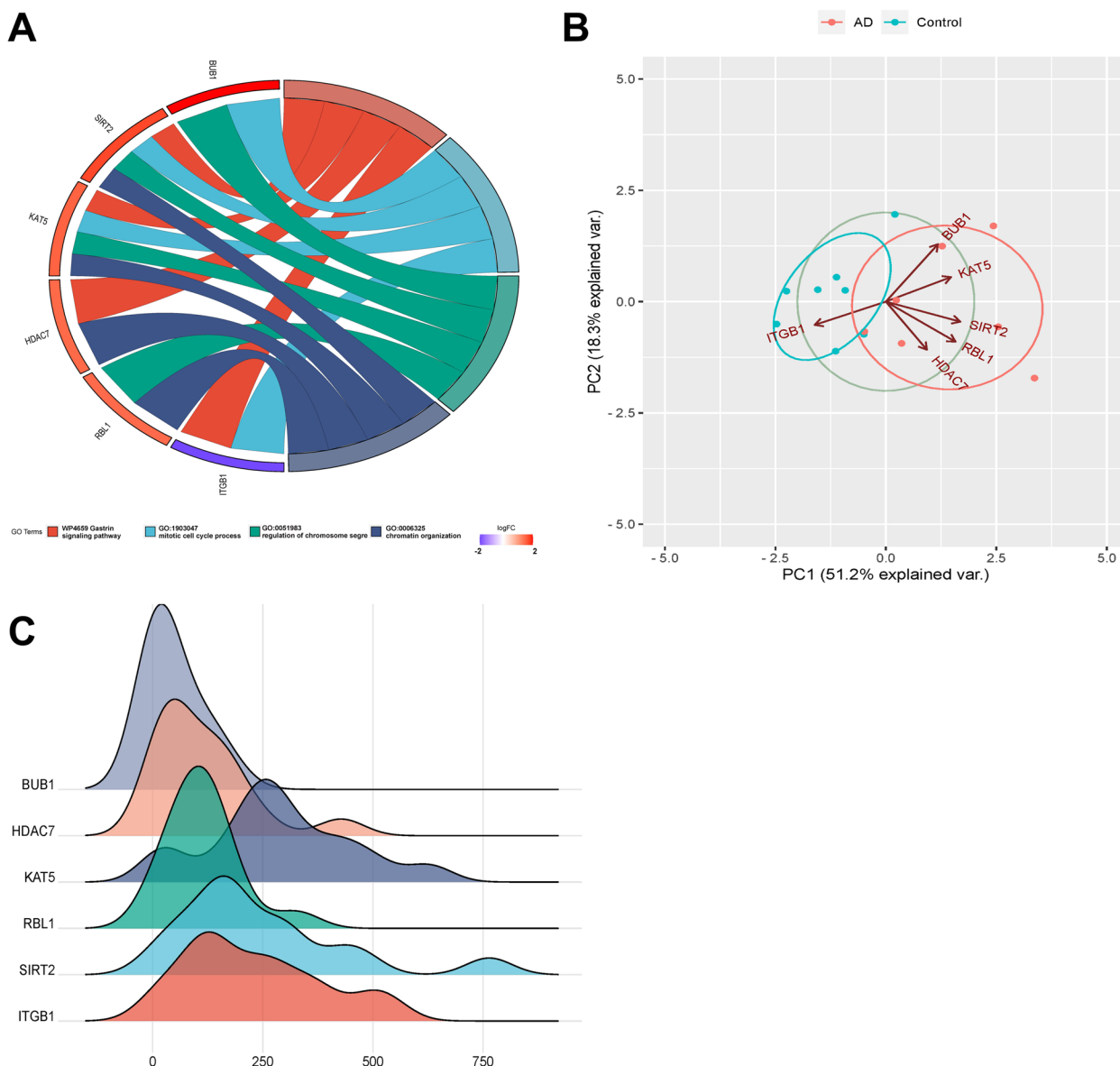


**Fig. 4** Hub gene analysis **a** GO pathway diagram, consisting of three parts: genes, LogFold Change (representing the fold change of genes for sorting and color-coding gene blocks), and other columns representing GO terms. Different connections between genes indicate their involvement in specific GO terms. **b** Principal component analysis (PCA) plot. The coordinates PC1 and PC2 represent the first and second principal components (i.e., latent variables explaining the differences). Points represent samples, and different colors represent different groups. **c** Gene ridge plot. The x-axis represents gene expression levels, and the shape of the ridges represents the distribution of data within each group, with the height indicating the number of samples corresponding to the gene expression level

GSE28146 dataset, with the true positive rates of 83.9, 82.1, 85.7, 92.9, 85.7, and 82.15%, respectively (Fig. 5). The true positive rates of ROC curves plotted using raw data from GSE5281 dataset of hub genes were 82.3, 88.5, 81.5, 90.8, 80.8, and 94.6%, respectively, which showed a distinguishing capacity of hub genes expression levels between AD samples and healthy controls (Fig. 6).

**HE staining**

The size, density, and arrangement of cortical nerve cells suggested the extent of neuron damage. In the control group, the cortical nerve cells of the mice brain tissue were densely organized, with full nucleoli and clear boundaries, which were in normal shape without pathological features. On the contrary, marked neuronal damage was observed in the mice of the model group. The cortical nerve cells of the model mice were overstained, loosely arranged, and their cytoplasm deformed and swollen, showing more lesions and irregular cell boundaries, which represented successful establishment of AD mice model (Fig. 7).

**RT-qPCR**

The results indicated that compared to the control group, the mRNA expression levels of *RBL1*, *BUB1*, *HDAC7*, *KAT5*, and *SIRT2* in the model group were significantly increased, while the mRNA expression level of *ITGB1* was significantly decreased, consisting with the prediction of bioinformatics analysis (Fig. 8).

**Discussion**

Currently, the treatment for AD can only alleviate its symptoms, which cannot suppress the progression of neurodegeneration and there is no effective treatment for people with AD [14]. Some oncogenes and suppressor genes have been found to be novel gene signatures for AD diagnosis [15, 16]. In this research, we identified 6 hub genes from PPI network based on 2 gene expression profiles related to AD. We then verified the abnormal expression of hub genes in vivo by constructing a mouse model of AD. Our findings not only provided new genetic diagnostic strategies, but also pointed the way to further study disease pathogenesis and therapeutic targets of AD.

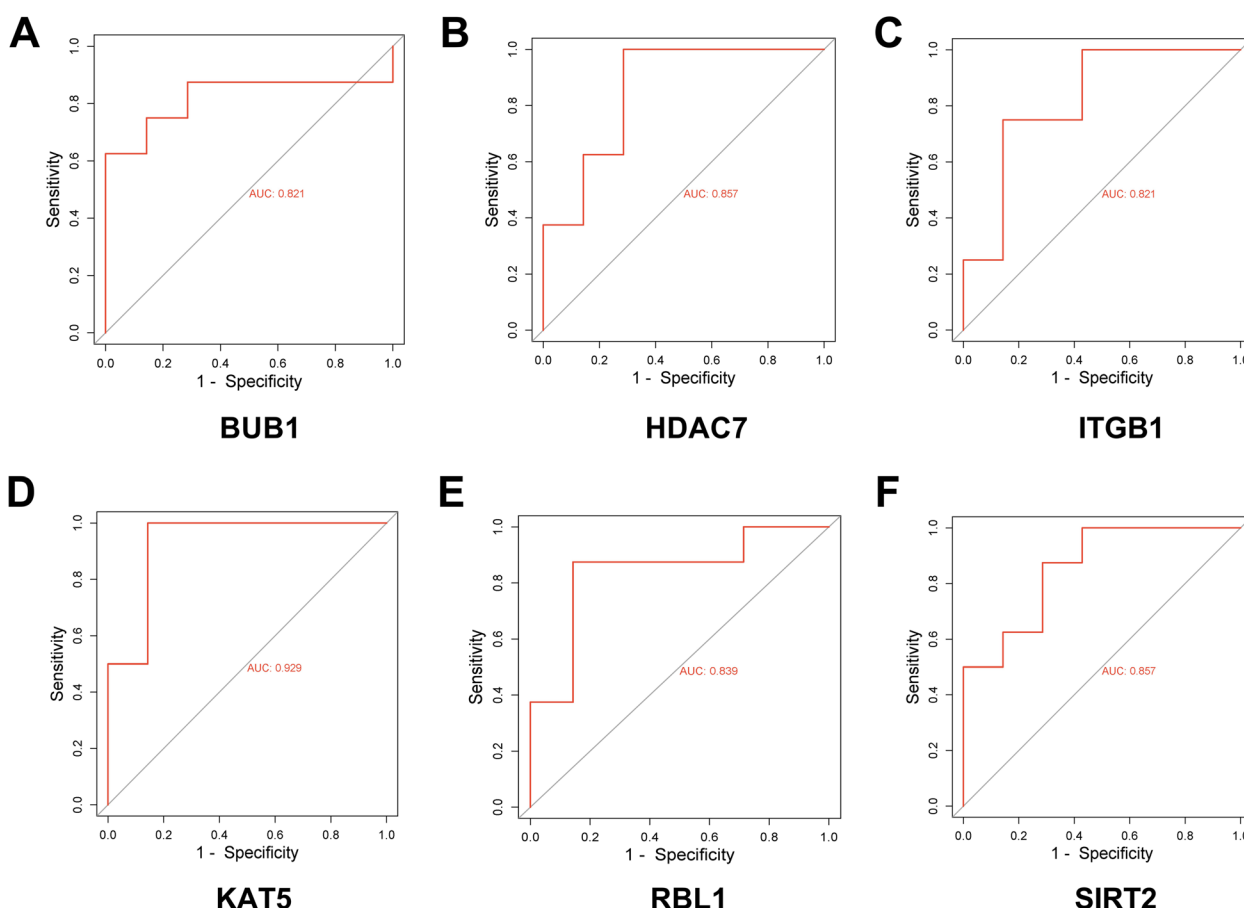


**Fig. 5** Receiver operating characteristic (ROC) curve plotted using the expression level of hub gene in GSE28146 dataset. **a-f** ROC analysis plots for genes *RBL1*, *BUB1*, *HDAC7*, *KAT5*, *SIRT2*, and *ITGB1*. The x-axis in ROC curve represents the false positive rate, the y-axis represents the true positive rate

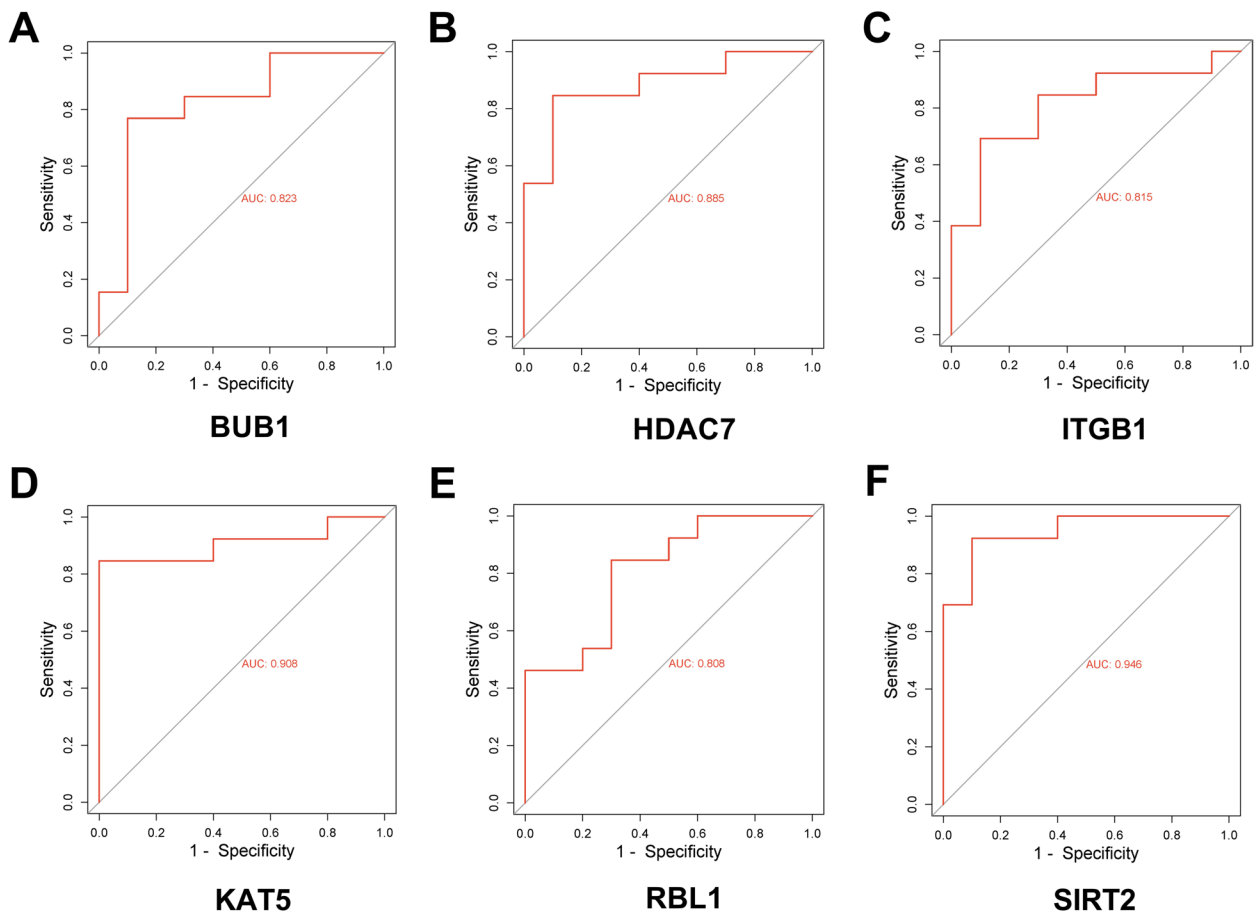


**Fig. 6** ROC curve plotted using the expression level of hub gene in GSE5281 dataset. **a-f** ROC analysis plots for genes *RBL1*, *BUB1*, *HDAC7*, *KAT5*, *SIRT2*, and *ITGB1*. The x-axis in ROC curve represents the false positive rate, the y-axis represents the true positive rate

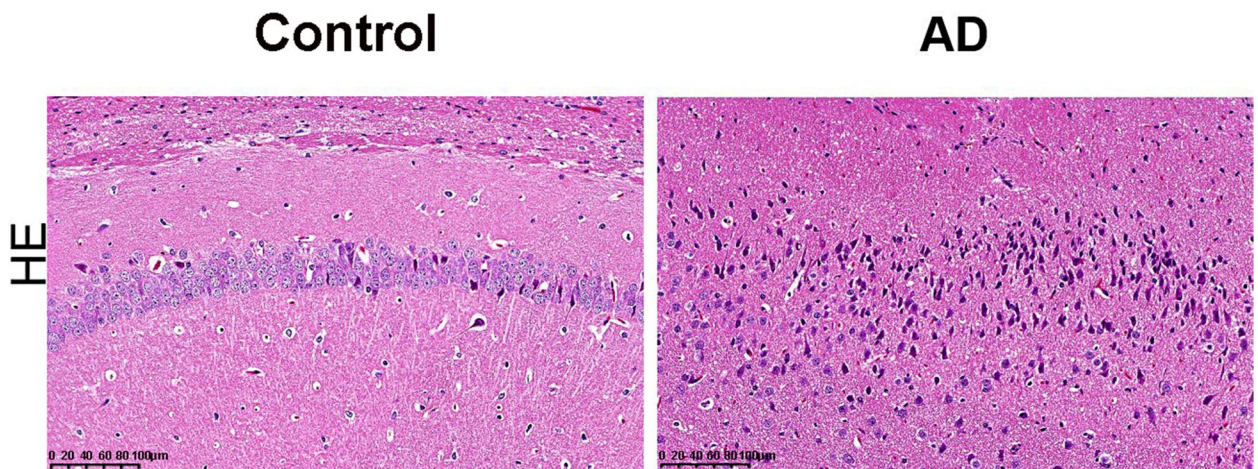


**Fig. 7** Hematoxylin-eosin staining results of brain tissues from AD mouse model (Magnification: 20X, scale: 100µm)

*RBL1*, *BUB1*, *HDAC7*, *KAT5*, *SIRT2* and *ITGB1* have been identified as key genes in various diseases. By analyzing the clinical data of 4 glioma patients in Affymetrix

chip, *RBL1* is isolated as a core gene affecting glioma patient survival and chemotherapy sensitivity [17]. *BUB1* is a gene signature that have a key effect on glioma stem

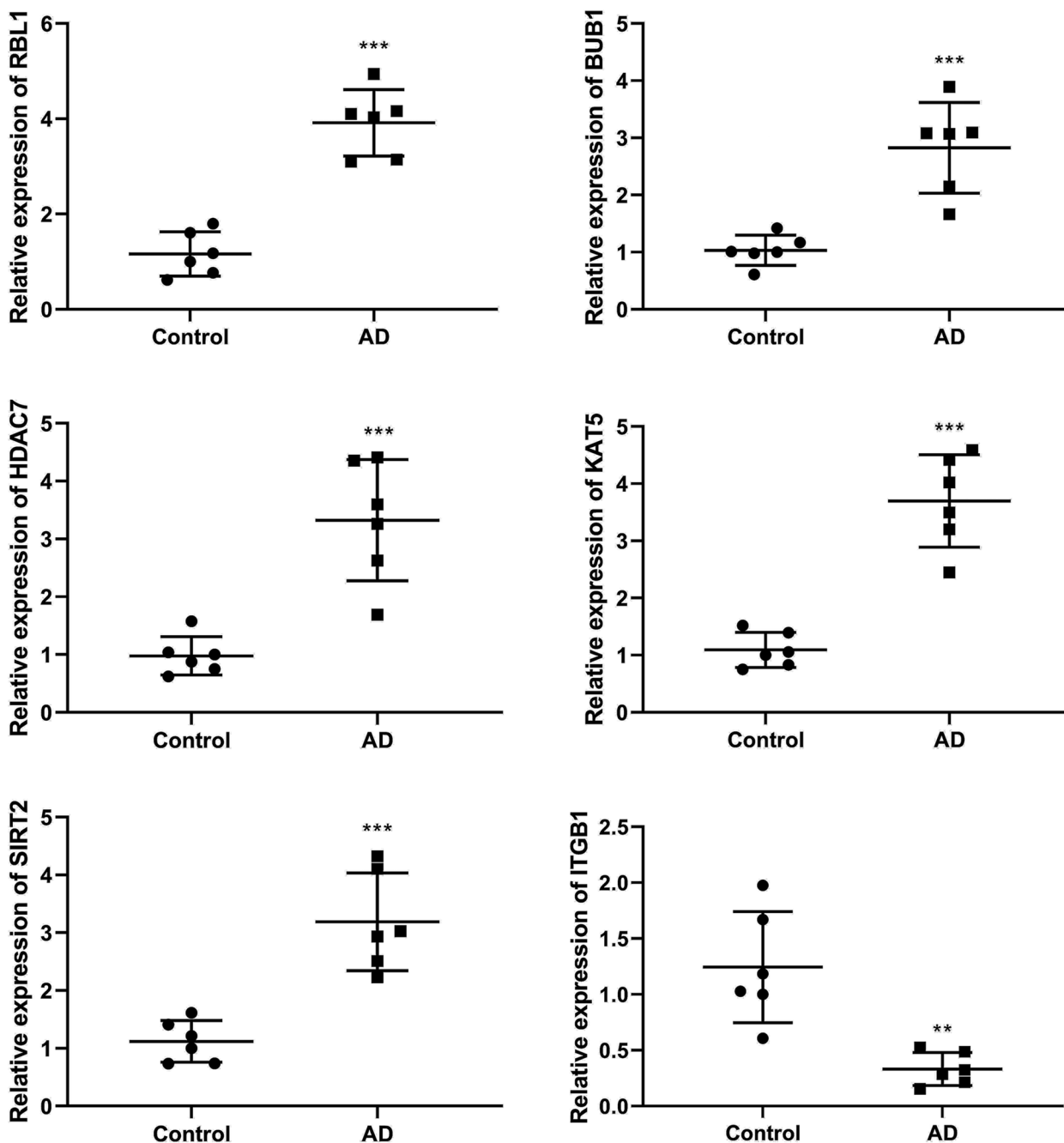


**Fig. 8** The mRNA expression levels of *RBL1*, *BUB1*, *HDAC7*, *KAT5*, *SIRT2*, and *ITGB1* detected by Real-time quantitative PCR. \*\* $P < 0.01$ , \*\*\* $P < 0.001$  vs. control group

cells after evaluating mRNA expression in glioma patient samples using The Cancer Genome Atlas and constructing DEGs co-expression networks of glioma samples by weighted gene co-expression network analysis [18]. Analysis of genomic data from 154 patients with glioblastoma multiforme has determined a strong correlation between *HDAC7* expression and patient outcomes:

Subgroup of patients with overexpressed *HDAC7* has particularly poor clinical outcomes [19]. To investigating the role of Tip60 (now called *KAT5*) in human glioma malignant behavior, RT-qPCR analysis of fresh human brain tumor tissues from 55 patients shows that decreased *KAT5* expression is associated with advanced glioma, which is an important candidate gene for glioma

[20]. Cerebrospinal fluid samples from patients with mild cognitive impairment caused by AD and a control group (i.e., patients with other neurological disorders) are analyzed using machine learning approaches, which identify *SIRT2* with high differential performance and can be used as a novel biomarker of neuroinflammation in AD [21]. After analyzing the datasets downloaded from GEO database to screen DEGs, performing GO and pathway enrichment analysis, constructing PPI, TF-target gene and miRNA-target gene networks, *ITGB1* is one of the hub genes that have been identified as possible targets for AD diagnosis and treatment [22]. In our research, after analyzing GSE5281 and GSE28146 datasets, *RBL1*, *BUB1*, *HDAC7*, *KAT5*, *SIRT2* and *ITGB1* were screened out with high predictive value, which might be important diagnostic markers for AD.

*RBL1* can inhibit the cell cycle and act as a disease suppressor [23–25]. In glioma, the expression level of *RBL1* is markedly down-regulated in glioma samples, playing a crucial role in glioma tumorigenesis [26]. *BUB1* is a mitotic kinase whose overexpression leads to aneuploidy, resulting in brain aging in health and disease [27, 28]. Compared with normal control tissues, *BUB1* expression is significantly up-regulated in glioblastoma multiforme samples [29]. *HDAC7* is a kind of histone deacetylases, and some histone deacetylases are associated with memory impairment and dementia [30–32]. *HDAC7* expression is up-regulated in malignant glioma, colorectal cancer, choroidal melanoma and other diseases [33–35]. *KAT5* acetylates and activates p53, which plays an important role in various cellular functions, associated with ageing-related diseases, including AD [36]. Transcriptomic analysis using the childhood cerebral cortex cell line as a neuronal model of novel coronavirus infection finds a decreased mRNA expression level of *KAT5* [37]. *SIRT2* is a sirtuin that is involved in aging, autophagy and inflammation, etc. [38, 39]. The expression level of *SIRT2* is up-regulated in brains of an insulin-deficient amyloid- $\beta$  precursor protein transgenic mouse [40]. Additionally, the expression level of *ITGB1* in an orthotopic xenograft model of invasive glioblastoma is down-regulated [41]. In the brain tissue of a mouse model of AD that we constructed, the mRNA levels of *RBL1*, *BUB1*, *HDAC7*, *KAT5*, and *SIRT2* significantly increased, while the mRNA level of *ITGB1* significantly decreased. In conclusion, *RBL1*, *BUB1*, *HDAC7*, *KAT5*, *SIRT2*, and *ITGB1* were involved in AD, which were the crucial biomarkers for AD.

All in all, the identification of key hub gene of AD using bioinformatics techniques is the main focus in this study. Among the DEGs, 6 hub genes, *RBL1*, *BUB1*, *HDAC7*, *KAT5*, *SIRT2*, and *ITGB1* were acquired.

Their abnormal expression was verified in vivo using AD mouse model. These hub genes have the potential to be novel treatment targets and biomarkers for AD patients. It is believed that our discovery would considerably advance knowledge of the underlying molecular mechanisms and causes of AD.

## Supplementary Information

The online version contains supplementary material available at <https://doi.org/10.1186/s12920-023-01775-6>.

**Additional file 1: Table S1.** The primer sequences.

**Additional file 2: Fig. S1.** Protein-protein interactions (PPI) network and key gene modules: Fig. A: PPI of DEGs. Fig. B: Hub genes identified using MCODE analysis. The lines between nodes represent the interactions between genes.

## Acknowledgements

Not applicable.

## Authors' contributions

Wenyuan Cao: Conception, design and analysis of data, performed the data analyses and wrote the manuscript; Zhangge Ji, Shoulian Zhu, Mei Wang and Running Sun: Performed the data analyses and wrote the manuscript; All authors have read and approved the manuscript.

## Funding

Not applicable.

## Availability of data and materials

The Gene expression profiles GSE5281 and GSE28146 analyzed during the current study are available in the Gene Expression Omnibus database at <https://www.ncbi.nlm.nih.gov/geo/query/acc.cgi?acc=GSE28146>, respectively.

## Declarations

### Ethics approval and consent to participate

The animal experiments were approved by the ethics committee of Zibo Municipal Hospital.

All methods were carried out in accordance with relevant guidelines and regulations. The study was reported in accordance with ARRIVE guidelines.

### Consent for publication

Not applicable.

### Competing interests

The authors declare no competing interests.

Received: 13 July 2023 Accepted: 12 December 2023

Published online: 02 January 2024

## References

- Li JM, Hu T, Zhou XN, Zhang T, Guo JH, Wang MY, Wu YL, Su WJ, Jiang CL. The involvement of NLRP3 inflammasome in CUMS-induced AD-like pathological changes and related cognitive decline in mice. *J Neuroinflammation*. 2023;20(1):112. <https://doi.org/10.1186/s12974-023-02791-0>.
- Alzheimer's Association. 2021 Alzheimer's disease facts and figures. *Alzheimers Dement*. 2021;17(3):327–406. <https://doi.org/10.1002/alz.12328>.
- Alzheimer's Association. 2023 Alzheimer's disease facts and figures. *Alzheimers Dement*. 2023;19(4):1598–695. <https://doi.org/10.1002/alz.13016>.
- Prince M, Wimo A, Guerchet M, Ali GC, Prina M. World Alzheimer report 2015. The global impact of dementia. An Analysis of Prevalence, Incidence, Cost and Trends; 2015.

5. Fang EF, Hou Y, Palikaras K, Adriaanse BA, Kerr JS, Yang B, Lautrup S, Hasan-Olive MM, Caponio D, Dan X, Rocktäschel P, Croteau DL, Akbari M, Greig NH, Fladby T, Nilsen H, Cader MZ, Mattson MP, Tavernarakis N, Bohr VA. Mitophagy inhibits amyloid- $\beta$  and tau pathology and reverses cognitive deficits in models of Alzheimer's disease. *Nat Neurosci*. 2019;22(3):401–12. <https://doi.org/10.1038/s41593-018-0332-9>.
6. Khan S. Recent advancements in pathogenesis, Diagnostics and Treatment of Alzheimer's Disease. 2020;18(11):1106–25. <https://doi.org/10.2174/1570159x18666200528142429>.
7. Xie J, Hoেকে LV, Vandenbroucke RE. The impact of systemic inflammation on Alzheimer's disease pathology. *Front Immunol*. 2021;12:796867.
8. Kinney JW, Bemiller SM, Murtishaw AS, Leisgang AM, Salazar AM, Lamb BT. Inflammation as a central mechanism in Alzheimer's disease. *Alzheimer's & Dementia: Translational Research & Clinical Interventions*. 2018;4(1)
9. Elena RV, Laure SA, Carter SF, Ove A, Karim F, Michael S, Konstantinos C, Steinunn T, Caroline K, Anders W. Diverging longitudinal changes in astrogliosis and amyloid PET in autosomal dominant Alzheimer's disease. *Brain*. 2016;39:awv404.
10. Breijyeh Z, Karaman R. Comprehensive review on Alzheimer's disease: causes and treatment. *Molecules*. 2020;25(24) <https://doi.org/10.3390/molecules25245789>.
11. Zhao K, Wu Y, Zhao D, Zhang H, Lin J, Wang Y. Six mitophagy-related hub genes as peripheral blood biomarkers of Alzheimer's disease and their immune cell infiltration correlation. *Front Neurosci*. 2023;17:1125281. <https://doi.org/10.3389/fnins.2023.1125281>.
12. Guan F, Gao Q, Dai X, Li L, Bao R, Gu J. LncRNA RP11-59J16.2 aggravates apoptosis and increases tau phosphorylation by targeting MCM2 in AD. *Front Genet*. 2022;13:824495. <https://doi.org/10.3389/fgene.2022.824495>.
13. Li H, Zou L, Shi J, Han X. Bioinformatics analysis of differentially expressed genes and identification of a miRNA-mRNA network associated with entorhinal cortex and hippocampus in Alzheimer's disease. *Heredity*. 2021;158(1):25. <https://doi.org/10.1186/s41065-021-00190-0>.
14. Sosa-Ortiz AL, Acosta-Castillo I, Prince MJ. Epidemiology of dementias and Alzheimer's disease. *Arch Med Res*. 2012;43(8):600–8.
15. Dai L, Wang Q, Lv X, Gao F, Chen Z, Shen Y. Elevated  $\beta$ -secretase 1 expression mediates CD4+ T cell dysfunction via PGE2 signalling in Alzheimer's disease. *Brain Behav Immun*. 2021;98:337–48. <https://doi.org/10.1016/j.bbi.2021.08.234>.
16. Li S, Qu L, Wang X, Kong L. Novel insights into RIPK1 as a promising target for future Alzheimer's disease treatment. *Pharmacol Ther*. 2022;231:107979. <https://doi.org/10.1016/j.pharmthera.2021.107979>.
17. Zhao Z, Liu Y, He H, Chen X, Chen J, Lu YC. Candidate genes influencing sensitivity and resistance of human glioblastoma to Semustine. *Brain Res Bull*. 2011;86(3–4):189–94. <https://doi.org/10.1016/j.brainresbull.2011.07.010>.
18. Xia P, Li Q, Wu G, Huang Y. Identification of glioma Cancer stem cell characteristics based on weighted gene prognosis module co-expression network analysis of transcriptome data Stemness indices. *J Mol Neurosci*. 2020;70(10):1512–20. <https://doi.org/10.1007/s12031-020-01590-z>.
19. Peixoto P, Blomme A, Costanza B, Ronca R, Rezzola S, Palacios AP, Schoysman L, Boutry S, Goffart N, Peulen O, Maris P, Di Valentin E, Hennequière V, Bianchi E, Henry A, Meunier P, Rogister B, Muller RN, Delvenne P, Bellahcène A, Castronovo V, Turtoi A. HDAC7 inhibition resets STAT3 tumorigenic activity in human glioblastoma independently of EGFR and PTEN: new opportunities for selected targeted therapies. *Oncogene*. 2016;35(34):4481–94. <https://doi.org/10.1038/ncr.2015.506>.
20. Takino T, Nakada M, Li Z, Yoshimoto T, Domoto T, Sato H. Tip60 regulates MT1-MMP transcription and invasion of glioblastoma cells through NF- $\kappa$ B pathway. *Clin Exp Metastasis*. 2016;33(1):45–52. <https://doi.org/10.1007/s10585-015-9756-8>.
21. Gaetani L, Bellomo G, Parnetti L, Blennow K, Zetterberg H, Di Filippo M. Neuroinflammation and Alzheimer's disease: a machine learning approach to CSF proteomics. *Cells*. 2021;10(8) <https://doi.org/10.3390/cells10081930>.
22. Cheng Y, Sun M, Wang F, Geng X, Wang F. Identification of hub genes related to Alzheimer's disease and major depressive disorder. *Am J Alzheimer's Dis Other Dement*. 2021;36:15333175211046123. <https://doi.org/10.1177/15333175211046123>.
23. Henley SA, Dick FA. The retinoblastoma family of proteins and their regulatory functions in the mammalian cell division cycle. *Cell Div*. 2012;7
24. Sadasivam S, Decaprio JA. The DREAM complex: master coordinator of cell cycle-dependent gene expression. *Nat Rev Cancer*. 2013;13(10):585.
25. Perampalam P, Hassan HM, Lilly GE, Passos DT, Dick FA. Disrupting the DREAM transcriptional repressor complex induces apolipoprotein overexpression and systemic amyloidosis in mice. *J Clin Invest*. 2021;
26. Liu F, Gong J, Huang W, Wang Z, Wang M, Yang J, Wu C, Wu Z, Han B. MicroRNA-106b-5p boosts glioma tumorigenesis by targeting multiple tumor suppressor genes. *Oncogene*. 2014;33(40):4813–22. <https://doi.org/10.1038/onc.2013.428>.
27. Ricke RM, van Deursen JM. Aurora B hyperactivation by Bub1 overexpression promotes chromosome missegregation. *Cell Cycle*. 2011;10(21):3645–51. <https://doi.org/10.4161/cc.10.21.18156>.
28. Iourov IY, Yurov YB, Vorsanova SG, Kutsev SI. Chromosome instability, aging and brain diseases. *Cells*. 2021;10(5) <https://doi.org/10.3390/cells10051256>.
29. Chen X, Pan Y, Yan M, Bao G, Sun X. Identification of potential crucial genes and molecular mechanisms in glioblastoma multiforme by bioinformatics analysis. *Mol Med Rep*. 2020;22(2):859–69. <https://doi.org/10.3892/mmr.2020.11160>.
30. Kabir F, Atkinson R, Cook AL, Phipps AJ, King AE. The role of altered protein acetylation in neurodegenerative disease. *Front Aging Neurosci*. 2022;14:1025473. <https://doi.org/10.3389/fnagi.2022.1025473>.
31. Kumar V, Kundu S, Singh A, Singh S. Understanding the role of histone deacetylase and their inhibitors in neurodegenerative disorders: current targets and future perspective. *Curr Neuropharmacol*. 2022;20(1):158–78. <https://doi.org/10.2174/1570159x19666210609160017>.
32. Sharma S, Sarathlal KC, Taliyan R. Epigenetics in neurodegenerative diseases: the role of histone deacetylases. *CNS Neurol Disord Drug Targets*. 2019;18(1):11–8. <https://doi.org/10.2174/1871527317666181004155136>.
33. Was H, Krol SK, Rotili D, Mai A, Wojtas B, Kaminska B, Maleszewska M. Histone deacetylase inhibitors exert anti-tumor effects on human adherent and stem-like glioma cells. *Clin Epigenetics*. 2019;11(1):11. <https://doi.org/10.1186/s13148-018-0598-5>.
34. Stypula-Cyrus Y, Damanian D, Kunte DP, Cruz MD, Subramanian H, Roy HK, Backman V. HDAC up-regulation in early colon field carcinogenesis is involved in cell tumorigenicity through regulation of chromatin structure. *PLoS One*. 2013;8(5):e64600. <https://doi.org/10.1371/journal.pone.0064600>.
35. Zhang Y, Ding P, Wang Y, Shao C, Guo K, Yang H, Feng Y, Ning J, Pan M, Wang P, Yan X, Ma Z, Han J. HDAC7/c-Myc signaling pathway promotes the proliferation and metastasis of choroidal melanoma cells. *Cell Death Dis*. 2023;14(1):38. <https://doi.org/10.1038/s41419-022-05522-0>.
36. Lanni C, Racchi M, Memo M, Govoni S, Uberti D. P53 at the crossroads between cancer and neurodegeneration. *Free Radical Biology and Medicine: The Official Journal of the Oxygen Society*. 2012;52(9):1727–33.
37. Valeri A, Chiricosta L, Calcaterra V, Biasin M, Cappelletti G, Carelli S, Zucotti GV, Bramanti P, Pelizzo G, Mazzon E. Transcriptomic analysis of HCN-2 cells suggests connection among oxidative stress, senescence, and neuron death after SARS-CoV-2 infection. *Cells*. 2021;9
38. Puigoriol-Illamola D, Martínez-Damas M, Griñán-Ferré C, Pallàs M. Chronic mild stress modified epigenetic mechanisms leading to accelerated senescence and impaired cognitive performance in mice. *Int J Mol Sci*. 2020;21(3) <https://doi.org/10.3390/ijms21031154>.
39. Lu W, Wang Q, Xu C, Yuan H, Fan Q, Chen B, Cai R, Wu D, Xu M. SUMOylation is essential for Sirt2 tumor-suppressor function in neuroblastoma. *Neoplasia*. 2021;23(1):129–39. <https://doi.org/10.1016/j.neo.2020.11.013>.
40. Zhou C, Jung CG, Kim MJ, Watanabe A, Abdelhamid M, Taslima F, Michikawa M. Insulin deficiency increases Sirt2 level in Streptozotocin-treated Alzheimer's disease-like mouse model: increased Sirt2 induces tau phosphorylation through ERK activation. *Mol Neurobiol*. 2022;59(9):5408–25. <https://doi.org/10.1007/s12035-022-02918-z>.
41. Barrette AM, Ronk H, Joshi T, Mussa Z, Mehrotra M, Bouras A, Nudelman G, Jesu Raj JG, Bozec D, Lam W, Houldsworth J, Yong R, Zaslavsky E, Hadjipapanayis CG, Birtwistle MR, Tsankova NM. Anti-invasive efficacy and survival benefit of the YAP-TEAD inhibitor verteporfin in preclinical glioblastoma models. *Neuro-Oncology*. 2022;24(5):694–707. <https://doi.org/10.1093/neuonc/noab244>.

## Publisher's Note

Springer Nature remains neutral with regard to jurisdictional claims in published maps and institutional affiliations.